RESEARCH ARTICLE

ESPL **WILEY**

The influence of bedrock river morphology and alluvial cover on gravel entrainment: Part 1. Pivot angles and surface roughness

Marcus E. H. Buechel[1] 🆔 | **Rebecca A. Hodge[2]** 🆔 | **Sophie Kenmare[2]**

[1]School of Geography and the Environment, University of Oxford, Oxford, UK

[2]Department of Geography, Durham University, Durham, UK

Correspondence
Rebecca A. Hodge, Department of Geography, Durham University, South Road, Durham, DH1 3LE, UK.
Email: rebecca.hodge@durham.ac.uk

Abstract

Sediment entrainment in bedrock rivers is a key process for river incision and landscape evolution. Bedrock riverbeds are typically comprised of both exposed bedrock and alluvial patches, meaning grains can be entrained from positions on both surfaces. The critical shear stress needed to entrain a grain will be affected by the topography that the grain is located on, as it determines grain pivot angle and exposure, and impacts the local flow profile. The aim of this pair of articles is to determine how the properties of bedrock surfaces with and without sediment cover affect the grain-scale geometry of sediment grains, and consequently their critical shear stress. We report experiments using 3D-printed scaled replicas of fluvial bedrock surfaces, with 0 to 100% additional sediment cover. For each surface, grain pivot angles were measured using a tilt table. In this first article, we report how surface roughness and grain pivot angle vary between surfaces and with different amounts of sediment cover, and we explore the relationship between pivot angles and different metrics for measuring surface roughness. We find that: (1) surface roughness is not necessarily a linear combination of the individual roughness of bedrock and alluvial areas, and the underlying bedrock topography can still influence surface roughness at 100% sediment cover; (2) pivot angles generally, but not always, decrease with increasing grain size relative to surface roughness; (3) changes in pivot angles with increasing sediment cover are best explained by changes in surface roughness at spatial scales comparable to the grain size; and (4) pivot angles are also best explained by roughness metrics that incorporate the direction of roughness with respect to the tilt direction, and the surface inclination. This work provides new insights into the processes behind grain entrainment in bedrock rivers that are critical for determining how landscapes may evolve.

KEYWORDS
3D printing, bedrock river, grain entrainment, pivot angle, surface roughness

1 | INTRODUCTION

Bedrock rivers are an integral component of the landscape system, providing a mechanism by which landscapes can respond to both external forcing such as rainfall, and internal forcing such as landslides (Brunsden & Thornes, 1979; Burbank et al., 1996; Harvey, 2001).

Bedrock rivers are those whereby changes in channel morphology require erosion of bedrock bed or banks, and where the bedrock may be covered by a mobile alluvial layer (Tinkler & Wohl, 1998; Turowski et al., 2008). Multiple factors influence bedrock erosion rates including lithology, precipitation, bedrock geometry and sediment cover (Hartshorn, 2002; Johnson et al., 2010; Montgomery & Gran, 2001;

Murphy et al., 2016; Sklar & Dietrich, 2001). The tool and cover, or saltation-abrasion, paradigm explains how sediment entrainment, transport, and deposition both causes and inhibits bedrock erosion, leading to changes in channel geomorphology (Gilbert, 1877; Sklar & Dietrich, 2001, 2004). A full understanding of these interactions therefore requires understanding of the processes by which sediment is both entrained and transported in bedrock rivers. The differing topography of exposed bedrock riverbeds compared to that of alluvial beds affects grain entrainment in at least two ways. Firstly, the bedrock surface influences the pocket geometry in which the grain is sitting and the position of the grain relative to the water velocity profile. Secondly, the roughness of the bedrock will affect the flow hydraulics. Neither effect is yet well understood. Furthermore, the presence of exposed bedrock with a thin alluvial veneer has been shown to cause sediment transport processes that are different to those in alluvial channels (Chatanantavet & Parker, 2008; Goode & Wohl, 2010; Hodge et al., 2011), but a good understanding of these interactions is lacking.

Grain entrainment occurs when the force applied by the flow exceeds the resisting forces of the grain. The magnitude of both forces depends on the grain geometry, that is the way in which the grain is positioned relative to other grains and/or the bedrock surface. This geometry is often described by a pivot angle (ϕ) (Shields, 1936), which is the angle through which a grain rotates in order to be entrained from its pocket. At the point of entrainment, the force balance along the pivot plane is:

$$F_D \cos \phi = F_W \sin \phi \tag{1}$$

where F_D is the drag force and F_W is the immersed weight of the grain, and lift forces are not considered. Assuming that the grain can move without obstruction, the pivot angle is (Johnston et al., 1998):

$$\tan \phi = \left(\frac{F_D}{F_W} \right) \tag{2}$$

Greater pivot angles represent larger forces required to mobilize a grain relative to its size. Pivot angles can be measured directly by placing a grain onto a surface and tilting the surface until the grain is displaced; the angle of the surface from the horizontal is equal to the pivot angle (Buffington et al., 1992; Li & Komar, 1986).

In alluvial settings, pivot angles have often been expressed as an inverse function of the size of the pivoting grain relative to the underlying grains (Johnston et al., 1998; Kirchner et al., 1990; Li & Komar, 1986; Prancevic & Lamb, 2015), although not all data show this relationship (Hodge et al., 2020). This relationship is expected because relatively larger grains generate rougher surfaces with deeper pockets and therefore higher pivot angles (Buffington et al., 1992; Johnston et al., 1998; Komar & Li, 1986). For grains on bedrock, we expect that pivot angles are dependent on the relative roughness of the surface compared to grain size. Bedrock surface roughness has been quantified using the standard deviation of elevations (σ_z, e.g., Johnson, 2014), however we do not know if this metric fully explains variations in pivot angles.

To gain a greater understanding of sediment entrainment in bedrock channels, we also need to know how surface roughness and pivot angles change as sediment cover develops. Sediment cover can make surfaces smoother or rougher depending on the ratio of bedrock roughness to grain size (Inoue et al., 2014), leading to an increase or decrease in pivot angles. However, this has not been tested. The impact of sediment cover on overall roughness is also important for predicting flow resistance. The overall roughness of bedrock surfaces with partial alluvial cover has been assumed to be a weighted average of the individual roughness of bedrock and alluvial areas (Inoue et al., 2014; Johnson, 2014; Nelson et al., 2014; Nelson & Seminara, 2012). This has been tested indirectly using hydraulic data (Ferguson et al., 2017; Johnson, 2014), but the impact of changing sediment cover on overall channel topography has not been measured directly.

The aim of this pair of articles is to determine how the properties of bedrock surfaces with and without sediment cover affect the grain-scale geometry of sediment grains, and consequently their critical shear stress for grain entrainment. In this initial article, we first report how surface properties and grain pivot angles vary between bedrock surfaces, and with different percentages (0–100%) of alluvial cover. The aims of this first article are to:

1. Ascertain the nature of surface roughness changes with increasing alluvial cover on bedrock riverbeds.
2. Report grain pivot angles across a range of bedrock surfaces with increasing alluvial cover.
3. Assess the relationships between recorded pivot angle and differing methods of surface roughness quantification.

We replicate bedrock surfaces in the laboratory by three-dimensional (3D) printing bedrock surfaces surveyed in the field using terrestrial laser scanning (TLS) and structure-from-motion (SfM) photogrammetry. We then use a tilt table to isolate the impact of pocket geometry on pivot angle for grains on bedrock and mixed bedrock-alluvial surfaces (Kirchner et al., 1990; Li & Komar, 1986). By measuring a single grain at a time, we ensure that the recorded pivot angle is determined only by the pocket geometry of the underlying bedrock morphology or alluvial cover. This allows us to reduce aleatory uncertainties generated by hydraulic processes in the field (e.g., turbulent sweeps and instantaneous pressure gradients in the water column; Schmeeckle et al., 2007; Vollmer & Kleinhans, 2007). In the companion article (Hodge & Buechel, 2022), we calculate critical shear stress by using the pivot angles and roughness values to parameterize the grain entrainment model of Kirchner et al. (1990), and we compare our results to entrainment models for bedrock rivers developed by Inoue et al. (2014) and Johnson (2014).

2 | METHODS

2.1 | Creation of bedrock surfaces

Bedrock morphology is a function of both eroding forces and substrate strength (Johnson et al., 2010; Wohl, 1992; Wohl & Merritt, 2001), and so bedrock channel morphology varies from smooth bedrock over which sediment grains can move easily (Ferguson et al., 2017; Tinkler & Wohl, 1998), to rough bedrock where sediment grain motion is inhibited (Goode & Wohl, 2010; Wilson et al., 2013). To represent this natural variability, we use natural

FIGURE 1 Photographs of the River Garry (top; 56°48′16″N 4°05′10″W, photographs from Richard Williams) and North Wash (bottom; 37°59′27″N 110°29′47″W) [Color figure can be viewed at wileyonlinelibrary.com]

bedrock surfaces with < 20% sediment cover from two rivers (Figure 1): North Wash in Utah, USA, and the River Garry in Scotland, UK (Reid, 2016; Williams et al., 2022). North Wash is a plane-bed river formed of sedimentary sandstone where shallow inner channel depressions and minor pitting of the surface is observed. The River Garry is formed of tilted, metamorphic rocks that have produced a stepped profile. The dominant bedding planes have created transverse ribs, which form large-scale morphologic form drag features which disrupt the flow (Lamb et al., 2017).

The 3D elevation data for North Wash and the River Garry were collected using SfM photogrammetry and TLS, respectively. Approximately 400 photographs of the North Wash were compiled using a handheld single-lens reflex camera (Nikon D7000) in October 2016. Flow conditions were very low, maximizing sub-aerial exposure of the bed. The photographs of North Wash were taken ensuring optimal lighting conditions, minimal atmospheric interference and focused upon the topography to ensure maximum accuracy (Javernick et al., 2014; Ružić et al., 2014). To improve the resolution of the final point clouds (PCs), photographs were collected with a high overlap of features within the imagery (cf. Rosnell & Honkavaara, 2012). Photographs were collected systematically from a grid of locations over the bed, at a height of approximately 1.5 m and at a variety of look angles to maximize coverage. Images out of focus or with low overlap with other images were removed. These photographs were used to construct 3D elevation data using SfM photogrammetry with Agisoft Photoscan (version 1.4.5) (e.g., Stumpf et al., 2015). Agisoft Photoscan uses a Scale Invariant Feature Transform algorithm to detect matching feature points between images of an object (Lowe, 2004). This algorithm allows calculation of a matrix for the image pair to produce an image connectivity graph, allowing camera parameters including their rotation, translation, and focal length to be found from the images (Snavely et al., 2008).

The 3D elevation data of the River Garry was generated in 2016 using TLS (Reid, 2016; Williams et al., 2022). Scans from multiple scan positions were registered together. We selected one area from the River Garry data (approximately 7 m by 7 m), and three from the North Wash data (each approximately 2 m by 2 m). Our experimental

focus is on the roughness of the surfaces relative to the size of the selected gravels, rather than trying to reproduce a specific field location at a certain scale, and so we did not apply a particular scale factor when converting from the PC to the printed surface. As bedrock surface roughness reflects multiple different factors, natural surfaces are likely to exhibit a large variation in roughness. Consequently, although our laboratory experiments may not represent the relationship between sediment size and roughness found at the field sites, they are likely to be representative of bedrock surfaces elsewhere.

To create meshes from the TLS and SfM PCs, a Poisson surface reconstruction (Kazhdan & Hoppe, 2013) with an octree depth of eight was undertaken in CloudCompare. Mesh scale was reduced so that the key topographic features were sufficiently represented across the printed area. Surface meshes were further edited using Autodesk NetFabb to produce a watertight solid for 3D printing. The final shapes were 0.27 m by 0.27 m in area, which is the maximum size that could be printed using a 'lulzbot taz 6' printer. Printing used PLA plastic and a 120 μm layer height. This thickness equates to 1 mm to 3 mm in the TLS and SfM data and is less than typical survey registration errors. Surfaces were sprayed with Ghiant Inkjet matt fixative to increase surface friction to be more similar to that of an unpolished rock surface. Four surfaces were initially produced: one rough from the River Garry (R1), two with medium roughness (M1 and M2) and one smooth (S1) from North Wash. Two more surfaces were produced from M2 and R1 by increasing the scale by 100% in all dimensions, creating surfaces $M2_{x2}$ and $R1_{x2}$. R1 has a strong directional structure, and we also tested R1 rotated through 90° (referred to as $R1_{rot}$), producing a total of seven surfaces (Figure 2).

2.2 | Measuring pivot angles

Pivot angles were measured using natural grains. Natural gravels predominantly between 8 mm and 32 mm in size were first washed to remove fine material which could alter their frictional properties. Gravels were sieved into four φ clast sizes: < 8 mm, 8–11.3 mm,
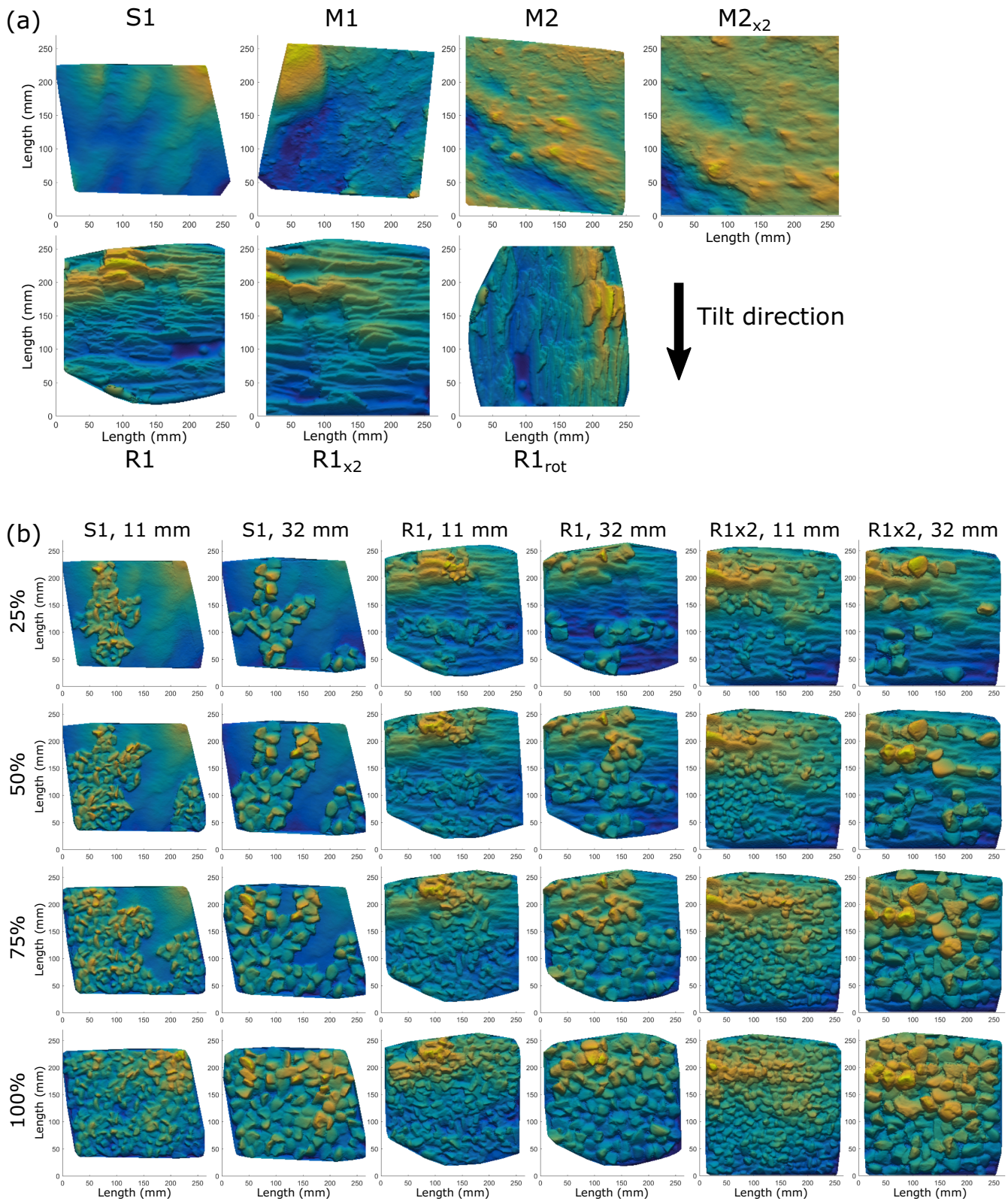
FIGURE 2 (a) Digital elevation models (DEMs) of surfaces used in the experiments and (b) DEMs surfaces with varying amounts of 11 or 32 mm sediment cover. Colour scale shows elevation and varies between surfaces to enhance visibility of the surface topography. Tilt direction indicates the downslope direction in the pivot angle experiments [Color figure can be viewed at wileyonlinelibrary.com]

11.3–16 mm and 16–32 mm (we refer to these as 8 mm, 11 mm, 16 mm and 32 mm grains, respectively). Twenty grains were randomly sub-sampled from each of the sieved clast sizes. There are a large number of indices that can be used to quantify particle shape, however we measured the three axes of each gravel in this sample to

allow an understanding of the basic geometry of the gravels used (Benn & Ballantyne, 1993).

To understand surface friction influence on clast mobility, sandpapers with particle diameters of 100 μm and 269 μm were attached to the tilt table. Sampled gravels were dropped from a height of about
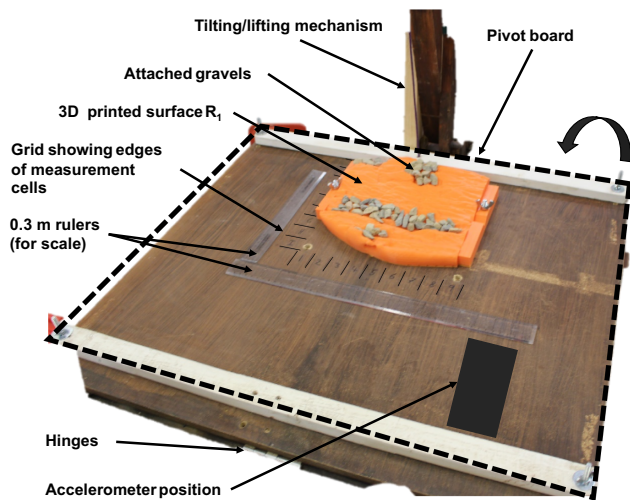
FIGURE 3 Experimental set-up of the tilt table. The grid markings drawn around the edge of the surface mark the locations of the 30 mm measurement cells [Color figure can be viewed at wileyonlinelibrary.com]

50 mm onto the sandpapers and the table tilted until the grain moved more than one grain diameter (Kirchner et al., 1990). The angle of the tilt table from the horizontal is the pivot angle. Each gravel was dropped and tilted five times on each sandpaper to calculate representative pivot angle values for each grain. Repeats are necessary because particle mobility should be treated as a probability distribution and no single value of pivot angle should be used to characterize particle mobilization (Buffington et al., 1992; Kirchner et al., 1990; Powell, 1998). Pivot angles were recorded to a tenth of a degree using the accelerometer of a Sony Xperia XZ and a Samsung Galaxy S2 phone placed level on the board. To determine accelerometer accuracy, the phone was tilted to various angles and basic trigonometric calculations were used (using measured opposite and adjacent lengths) to determine that the angle measured by the accelerometer was the observed angle. A significant agreement of $R^2 = 0.998$ ($t[10] = 0.95$, $p < 0.05$) was found between accelerometer recorded angle and actual angle. From the sandpaper analysis, a representative grain from each size range was chosen by selecting grains with roughly similar shapes and relatively low standard deviation between repeat measurements of pivot angles on the sandpaper surfaces. This ensures that later variations in pivot angles on the 3D printed surfaces reflect surface morphology rather than variations in clast properties. The b-axes of these grains are 12, 13.8, 16.9 and 20 mm, respectively. Some axes are larger than the sieve diameter, due to the limitations of size sorting with square sieve meshes. We only use one representative grain per size class to enable us to undertake the maximum number of repeat pivot measurements across all areas of each surface, and thus calculate a probability distribution of each grain size's mobility.

The 3D printed surfaces were attached to the pivot table and a nine-by-nine grid of 30 mm squares termed measurement cells, was drawn. These cells are equivalent to the size of the largest grains tested, and ensure that the entire surface was sampled (Figure 3). Pivot angles were measured in each measurement cell by dropping the grain from a height of about 20 mm onto the cell. The table was tilted until the grain moved more than one grain diameter and this process was repeated three times in each measurement cell. Pivot angles were measured for all four grain sizes on each of the seven surfaces.

To understand alluvial cover influence on pivot angles, varying amounts of 8–11.3 mm and 16–32 mm gravels (referred to as 11 mm and 32 mm gravels) were attached to surfaces S1, R1 and R1$_{x2}$ with PVA glue to produce 25, 50, 75 and 100% alluvial covere (Figure 2). The location of sediment cover was initially determined by placing sediment on the surfaces and shaking to observe where clasts settled. This replicates clasts naturally being deposited in the lowest bed elevations (Hodge & Hoey, 2016b; Johnson & Whipple, 2010). The amount of cover was determined by counting the number of measurement cells that were filled with sediment, and so the percentage cover is an indication rather than an exact value. At each percentage cover, pivot angles were measured three times in each measurement cell, using the representative grain of the same size as the alluvial cover. For each of the six combinations of gravel size (11 and 32 mm) and surface (S1, R1, R1$_{x2}$), we present five pivot angle distributions across 0, 25, 50, 75, and 100% alluvial cover.

To quantify how the alluvial cover changed the surface properties, PCs of the 3D printed bedrock surfaces with alluvial cover were created using SfM photogrammetry (Pearson et al., 2017). Occlusion can be a major issue in PC reconstruction of gravel deposits as it can create inaccurate grain pocket geometries (Bertin et al., 2015). To minimize this error, the image collection sampling ensured the maximum number of surface aspects were obtained. Images were acquired using a Canon 100D DSLR and a Canon PowerShot S90 without using either optical or digital zoom as this reduces the quality of generated PCs (Bertin et al., 2015). To reduce 'doming errors' on produced PCs, images were calibrated to consider camera lens type in Agisoft Photoscan (Carbonneau & Dietrich, 2017).

PCs of the surfaces with alluvial cover were created in the same manner as initial bedrock surface production and georeferenced using a known spatial scale. To quantify the error of these created PCs, we generated PCs of the flat table surface and calculated the standard deviation and root mean square error (RMSE) of elevations (Hugenholtz et al., 2013; James & Robson, 2014). This gave an average standard deviation of 0.58 mm and RMSE of 0.91 mm, with the former being 0.9 to 3.1% of the range of elevations of the alluvial surfaces.

2.3 | Surface roughness quantification

Multiple roughness indices have been used to quantify the topographic properties of alluvial and bedrock surfaces, including standard deviation, semi-variance, range and skewness of surface elevations (Butler et al., 2001; Hodge et al., 2009; Mao et al., 2011; Nikora et al., 1998; Powell et al., 2016; Robert, 1991). Many of these properties vary according to the scale at which they are calculated (Bertin et al., 2017; Butler et al., 2001; Hodge & Hoey, 2016a; Nikora et al., 1998; Robert, 1991). There is evidence that the standard deviation of elevations (σ_z) represents the flow resistance of a surface (Aberle & Smart, 2003; Durand et al., 2020), but we do not know which topographic properties and scales best explain the impact of surface topography on grain entrainment.

We calculate the properties of our surfaces from digital elevation models (DEMs) of all surfaces gridded at a 1 mm resolution (as shown in Figure 2). Following previous work (Hodge & Hoey, 2016a; Johnson, 2014; Kirchner et al., 1990; Powell et al., 2016), we mainly

use σ_z to describe surface roughness, which is normally calculated from the entire dataset of surface elevations. Here, we develop the application of σ_z by altering it to include the scale and direction of surface roughness, as we expect that pivot angles might be affected by bed roughness at certain spatial scales. We employ two different approaches to isolate specific spatial scales within the topography prior to calculating σ_z. The first approach is to apply a high pass filter to the surface topography, which retains only elements of the topography with wavelengths less than the specified cutoff length, and then calculate σ_z of the new topography. The second approach is to calculate σ_z within a square moving window across the topography, such that each calculation considers only a limited area of the surface. We produce a single roughness value ($\overline{\sigma}_{z\_sqwin}$) as the mean of σ_z from all the individual windows.

These two approaches do not consider the direction of the surface topography, and so we also apply a directional version of each of them, giving four ways in which we calculate types of σ_z, as shown in Table 1. For the first approach, we introduce a directionality by calculating σ_z along each row of the DEM in the tilt direction, and then taking the mean to produce a single roughness value ($\overline{\sigma}_{z\_dir}$). For the moving window approach, we use windows that have a variable length in the tilt direction and are one row of the DEM wide in the cross-tilt direction. Again, σ_z is calculated for each window, and the overall roughness, $\overline{\sigma}_{z\_1win}$ is the mean of these values.

By comparing the different types of σ_z to the pivot data, we can identify the best approach for determining bedrock influence on grain entrainment. We first look for relationships between the average pivot angle for the different surfaces and the roughness values calculated for each surface. We then, for each surface, compare the average pivot angle for each 30 mm measurement cell and the roughness of the surface within those cells.

We also test two further ways of measuring surface properties. Firstly, Zhang et al. (2015) suggest surface roughness should be quantified using the range of elevations, rather than the standard deviation. We recalculate the metrics in Table 1 using range (R_z) instead of standard deviation, and assess how this affects the relationships between surface properties and mean pivot angles.

Secondly, when analysing relationships between the pivot angle for each measurement cell and the surface properties of those cells, we evaluate whether the slope direction of the cell also influences the grain pivot angle. We quantify slope direction using an inclination index (I). For each point in the DEM, $I = 1$ if the adjacent point in the tilt direction has a higher elevation, and $I = 0$ if the adjacent point has a lower elevation, and $I = 0.5$ if the elevations are identical. The inclination index for the measurement cell is then the average of all of

these values ($\overline{I}$) and would be zero for a plane sloping in the tilt direction, and one for a plane sloping in the opposite direction. For each measurement cell, we combine $\overline{I}$ with the version of σ_z that has been calculated for that surface as:

$$\sigma_z I = \overline{I} \left(\sigma_z / \max(\sigma_z) \right) \tag{3}$$

where $\sigma_z I$ is the combined term, and $\max(\sigma_z)$ is the maximum σ_z value calculated across the 81 measurement cells for that surface. $\sigma_z I$ varies between 0 and 1; $\sigma_z I$ equals 1 represents the most resistance to grain motion; that is, the measurement cell has the highest σ_z and all points within the cell have an up-tilt slope.

3 | RESULTS

3.1 | Surface roughness of surfaces with and without sediment cover

Using the most common metric to characterize surface roughness, σ_z, R1$_{x2}$ is the roughest surface, and, despite our initial impressions of the surfaces, M2 is the smoothest ($\sigma_z = 2.8$ and 8.4 mm respectively, Figure 4). Inoue et al. (2014) define surfaces as being 'clast-rough' or 'clast-smooth' where the ratio of bedrock roughness to grain size is
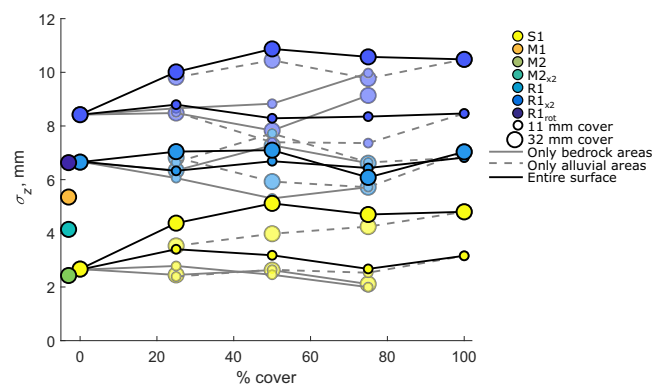
FIGURE 4 Standard deviation of surface elevations (σ_z) for each of the surfaces, under increasing amounts of sediment cover. Larger and smaller circles show fine and coarse (11 and 32 mm) cover respectively. Black solid lines show values for entire surface. Paler lines show roughness values for either only the sediment cover (dashed line) or the remaining exposed areas (solid line). Surfaces without any sediment cover experiments are shown to the left of % cover equals 0 [Color figure can be viewed at wileyonlinelibrary.com]

TABLE 1 Methods used to calculate different types of standard deviation of elevations (σz)

	Initial processing of the digital elevation model	σ_z Calculation	Directional?	Symbol
1	High pass filter	σ_z calculated using all DEM elevations	No	σ_z
2	High pass filter	σ_z calculated for each row of the DEM in the tilt direction, and all values of σ_z are then averaged	Yes	$\overline{\sigma}_{z\_dir}$
3	Use a square moving window and calculate σ_z within each window (σ_{z_sqwin})	Calculate mean of all values of σ_{z_sqwin}	No	$\overline{\sigma}_{z\_sqwin}$
4	Use a rectangular moving window with width = 1 mm in cross-tilt direction and calculate σ_z within each window (σ_{z_1win})	Calculate mean of all values of σ_{z_1win}	Yes	$\overline{\sigma}_{z\_1win}$

respectively greater or less than one, and bedrock roughness is back-calculated from hydraulic data. Following Johnson (2014) by using σ_z to quantify roughness indicates that all surfaces are 'clast-smooth' for all experimental grain sizes. In contrast, Zhang et al. (2015) define roughness using the range of elevations, in which case all surfaces are 'clast-rough' for the smaller two grain size classes, and only S1 and M2 are 'clast-smooth' for the larger two size classes.

Clast-rough and clast-smooth surfaces are expected to get respectively smoother and rougher with adding sediment cover (Inoue et al., 2014), with a larger change occurring when there is a larger difference between grain size and roughness. We would expect the largest change in σ_z when covering the smoothest surface (S1) with the largest (32 mm) grains. However, our results do not show this, with a cover of 32 mm grains causing similar increases in σ_z on both the smoothest (S1) and roughest (R1$_{x2}$) surfaces (i.e., clast-smooth behaviour), and not changing overall σ_z of the intermediate surface, R1 (Figure 4). Adding a cover of 11 mm grains does not change overall σ_z of any of the three surfaces. In four out of six cases (11 mm sediment on S1, and 32 mm sediment on S1, R1 and R1$_{x2}$), σ_z for the entire surface is higher than σ_z for just the alluvial or just the bedrock areas (Figure 4). This reflects a bimodal distribution in the surface elevations, with alluvial areas at one elevation range and bedrock areas at another, such that the overall σ_z is greater than that within each of the two ranges. Our data also show that the topography of the underlying surface still influences σ_z at 100% sediment cover; surfaces with 100% cover of the same grain size do not have the same σ_z (Figure 4).

The finding that adding sediment cover only increases total surface roughness in two out of six cases is surprising given that all surfaces were identified as clast-smooth. One possible explanation is that whether sediment cover alters overall σ_z also depends on the horizontal scales at which cover alters the bed topography. We test how sediment cover changes surface topography at different spatial scales by bandpass filtering the surfaces at a range of wavelengths and then calculating σ_z (termed σ_{z_BP}, Figure 5). A bandpass filter retains only topographic features with wavelengths within the specified range. Adding sediment cover increases σ_{z_BP} of all surfaces at the smallest 5–15, 15–25 and 25–35 mm wavelengths (Figure 5). For surfaces S1 and R1$_{x2}$, adding 25% or more 32 mm sediment cover (Figure 5d,f) also increases σ_{z_BP} at wavelengths greater than 35 mm, and so overall σ_z increases (as seen in Figure 4). For the other four cases (Figure 5a–c,e), adding 25% or more sediment cover either does not change, or reduces, σ_{z_BP} at wavelengths greater than 35 mm. These changes counteract the increase in σ_{z_BP} at wavelengths less than 35 mm, and so overall σ_z does not change (Figure 4). For example, with 11 mm cover on R1$_{x2}$ (Figure 5c), sediment cover increases σ_{z_BP} at wavelengths of 5 to 35 mm, but sediment infilling of bed hollows smooths the surface at wavelengths of 35 to 95 mm.

3.2 | Pivot angles on surfaces with and without sediment cover

From previous work we expect pivot angles to be higher for rougher surfaces, and/or smaller grains (Buffington et al., 1992; Johnston et al., 1998; Komar & Li, 1986). For surfaces with no sediment cover, pivot angles broadly follow this expected pattern, with smallest angles measured on the smoothest surface, S1, and highest angles measured on the rougher surfaces R1 and R1$_{x2}$ (Figure 6). However, the direction of the surface structure is important. Surface R1$_{rot}$ (where grains pivot parallel, instead of perpendicular, to the main bed structure) has
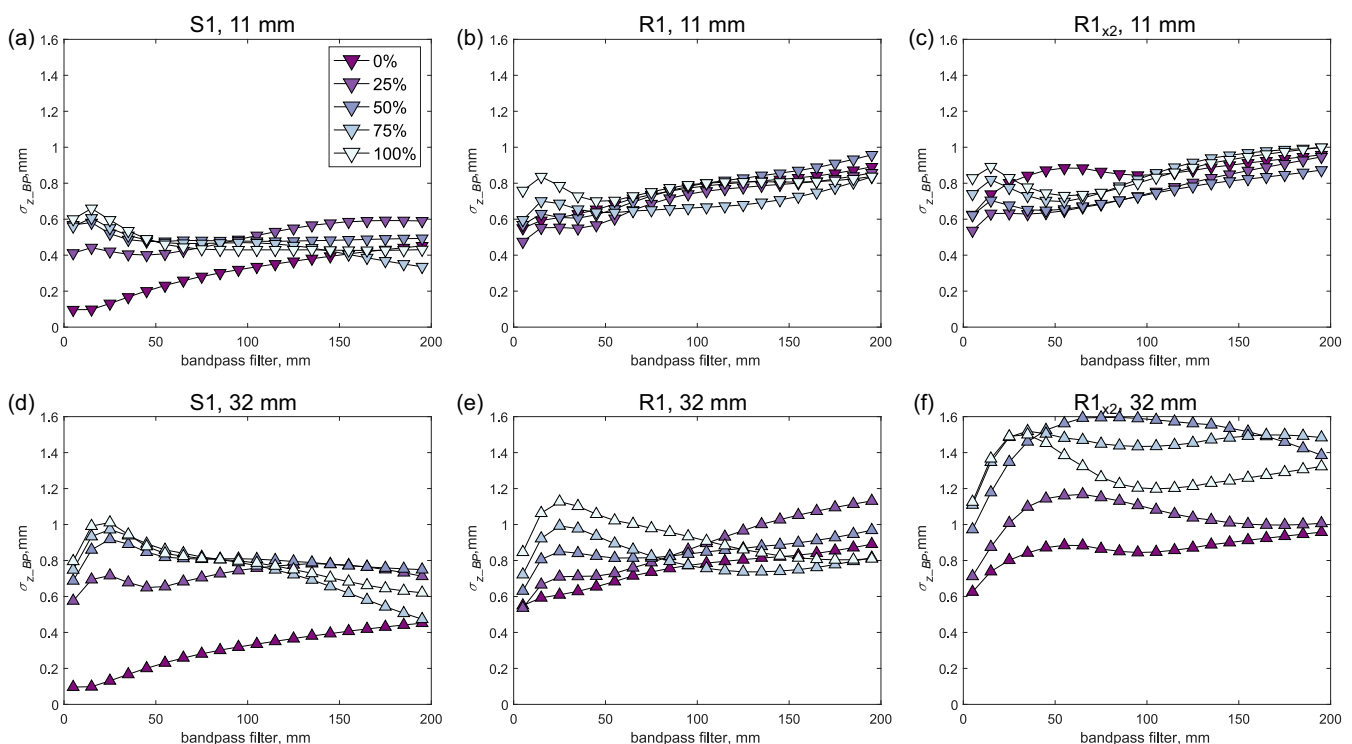
FIGURE 5 Standard deviation of elevations (σ_{z_BP}) of surfaces with different percentage cover after bandpass filtering at different wavelengths. All bandpass filters used a 10 mm range between lower and upper bands, and the x axis value is the lower band. Note that adding 32 mm sediment cover changes σ_z of the unfiltered surface for S1 and R1$_{x2}$, but not in the other four combinations of surface and grain size [Color figure can be viewed at wileyonlinelibrary.com]
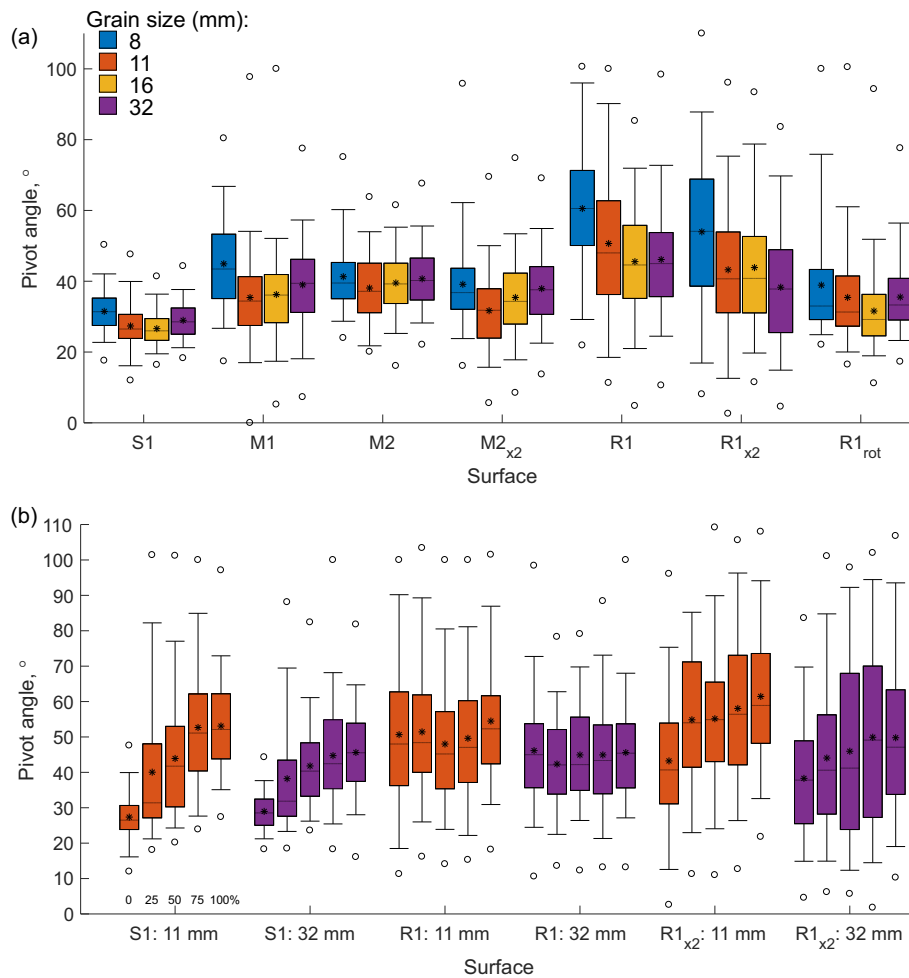
FIGURE 6 (a) Distributions of pivot angle for different grain sizes across the seven surfaces with no sediment cover. (b) Distributions of pivot angles on surfaces S1, R1 and R1$_{x2}$ with increasing levels of sediment cover. Colours refer to grain size of sediment cover and test grain. Box plot whiskers show 5th and 95th percentiles, and circles show minimum and maximum [Color figure can be viewed at wileyonlinelibrary.com]

lower pivot angles than surface R1, and similar angles to surfaces with medium roughness (Figure 6). Pivot angles vary inversely with grain size for surfaces R1, R1$_{x2}$ and to a lesser extent for S1 and R1$_{rot}$. M2 shows little variation with grain size, and M1 and M2$_{x2}$ show increasing pivot angles for some size fractions. Analysis of variance (ANOVA) shows that, for every surface, there is a significant difference ($p < 0.01$) between the mean pivot angles of the different grain sizes.

For the uncovered surfaces, pivot angles are generally higher on surfaces with higher σ_z. If adding sediment cover increases/decreases σ_z then pivot angles would also be expected to increase/decrease. This relationship is seen for four out of the six surface and sediment size combinations. For both 11 and 32 mm sediment on R1, σ_z is fairly constant for all amounts of sediment cover (Figure 4), and pivot angles also do not change (Figure 6b). For 32 mm cover on S1 and R1$_{x2}$, σ_z increases with sediment cover (Figure 4) and pivot angles also increase (Figure 6b). The exception is 11 mm grains on S1 and R1$_{x2}$, where σ_z does not vary with cover (Figure 4), but pivot angles increase (Figure 6b). This increase in pivot angles with sediment cover might be because adding sediment cover increases σ_z at smaller scales (e.g., σ_{z_BP} at wavelengths of 15 to 35 m in Figure 5), despite overall σ_z not changing.

For surfaces S1 and R1$_{x2}$, adding sediment cover not only increases the mean and median pivot angles, but also increases the range of pivot angles (Figure 6b). This is because sediment cover increases the variation in pocket geometries across the surface. At 100% sediment cover, it might be expected that the pivot angles

would just depend on the relative sizes of the cover and the pivoting grains. But, for both 11 and 32 mm cover, pivot angles are higher at 100% cover for R1$_{x2}$ than for the other two surfaces (Figure 6b), showing that the underlying bedrock topography continues to exert an influence.

3.3 | Pivot angles and alternative measures of surface roughness

The standard approach to predicting pivot angles is to relate average pivot angles to grain size divided by surface roughness, where surface roughness is characterized using the size of the underlying grains or σ_z. Plotted like this, our data are in line with previous studies (Figure 7). However, closer inspection shows cases where there are very different pivot angles for similar values of grain diameter/roughness (D/σ_z), specifically the pairs of S1 and M2, R1 and R1$_{rot}$, and S1 with and without sediment cover. However, R^2 of the relationship between mean pivot angle and D/roughness depends on which of the four methods (Table 1) is used to calculate roughness, and the window or filter size used in that calculation (Figure 8).

The strongest relationship between mean pivot angle and D/σ_z is produced when the surface roughness is characterized using $\overline{\sigma}_{z\_1win}$ (when standard deviation is calculated for every location using a rectangular moving window, and the mean of those values is then calculated; Figure 8a). The highest R^2 value occurs at the smallest window

FIGURE 7   Mean pivot angle (ϕ) as a function of D/σ_z or D/K_i, where D is grain size, σ_z is the standard deviation of surface elevations, and K_i is the underlying grain size. Red line shows power law fit to these data ($\phi = 56.9\,(D/\sigma_z)^{-0.256}$) and black lines show fit to other published datasets [Color figure can be viewed at wileyonlinelibrary.com]
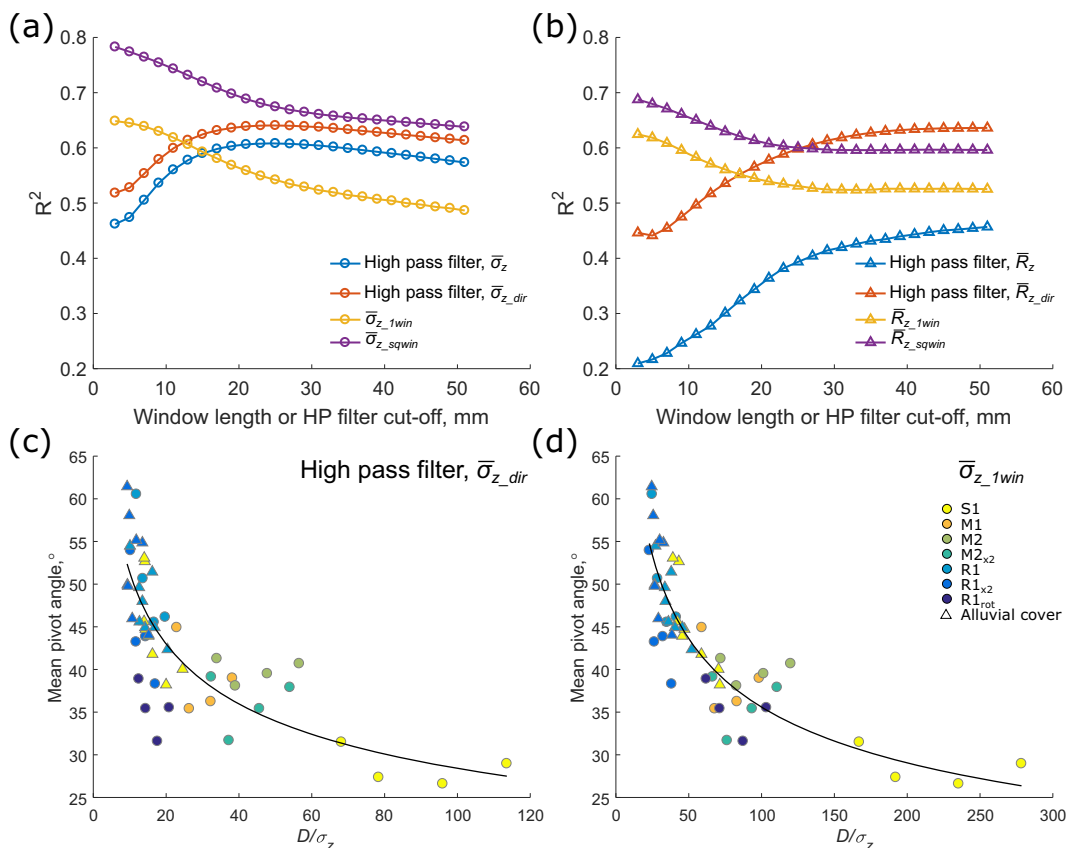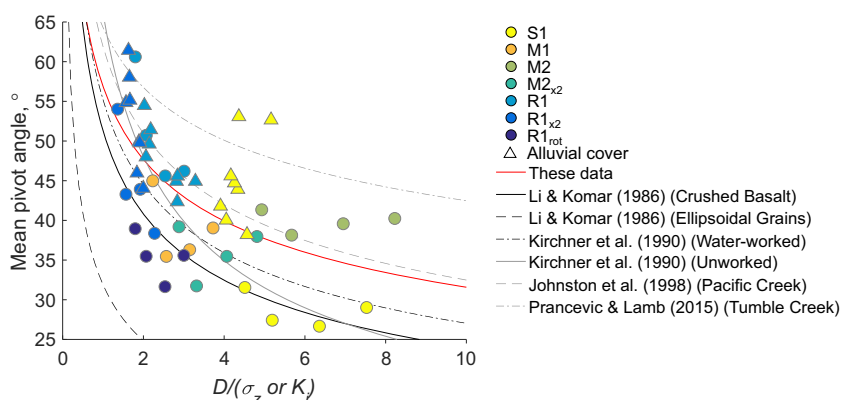
FIGURE 8   (a) The values of R^2 for the relationship between mean pivot angle and D/σ_z, where σ_z is calculated using the four different approaches outlined in Table 1. (b) The values of R^2 as before but using range instead of standard deviation to quantify surface roughness. (c) Best fit relationship between pivot angle and $D/\overline{\sigma}_{z\_dir}$ where the surfaces are initially filtered using a high-pass filter of 25 mm. (d) Best fit relationship between pivot angle and $D/\overline{\sigma}_{z\_1win}$ using a filter length of 3 mm [Color figure can be viewed at wileyonlinelibrary.com]

size of 3 mm length $\times$ 1 mm width. For both the rectangular and square windows, R^2 decreases with increasing window size (Figure 8a). Using $\overline{\sigma}_{z\_1win}$ is a better predictor of pivot angle than σ_z because, unlike σ_z, it produces different roughness values for each member of the pairs identified earlier (S1 and M2, R1 and R1$_{rot}$, and S1 with and without sediment cover; Figure 8d). However, values of $\overline{\sigma}_{z\_1win}$ are smaller than σ_z values, therefore any relationship will not be comparable to other studies (as in Figure 7). We also repeated this analysis using windows that were different widths but found that one-row-wide windows gave the highest R^2 correlation with pivot angles. Starting with a square window, decreasing the width relative to the length (i.e., a rectangle with the long axis parallel to the tilt

direction) increased R^2. But, increasing the width (i.e., a rectangle with the long axis perpendicular to the tilt direction) decreased the R^2 value. When we apply a high pass filter before calculating the standard deviation, R^2 is highest at a filter cutoff of 25 mm (Figure 8a), which is comparable to the size of the test grains. The value of R^2 is also higher when the standard deviation is calculated in the tilt direction.

Following Zhang et al. (2015), we also repeated our analysis using the range of elevations instead of the standard deviation. Using range for the entire surface (Figure 8b) gives a similar result to that shown in Figure 8(a); the similarity is because there is generally a high correlation between the range and the standard deviation. The

highest R^2 values are still produced using $\overline{R}_{z\_1win}$. The lowest are produced by R_z, which is the range metric that is most different to the equivalent metric using the standard deviation, which may reflect the fact that the range is very sensitive to any individual erroneous points in the DEM. Generally, this analysis suggests that the spatial scale that the roughness property is calculated over, and whether it is directional, is more important than whether it is the range or standard deviation.

3.4 | Pivot angles at the scale of the measurement cells

So far, we have analysed mean pivot angles, which we find depend on small-scale surface roughness along the tilt direction. Next, we looked at relationships between surface roughness and pivot angle at the scale of each of the 81 measurement cells. For each surface, we calculated the roughness of every measurement cell and calculated a power law relationship between D divided by these roughness values and the mean pivot angle measured in each cell (e.g., Figure 9b–d). We quantify roughness using σ_z (with no DEM processing) and $\overline{\sigma}_{z\_1win}$, selecting the latter because it gave the highest R^2 in Figure 8(a).

For $\overline{\sigma}_{z\_1win}$ we varied the window length between 3 and 31 mm. Figure 9(a) shows which combinations of surface and roughness metrics produce a power law relationship with an exponent that is significantly different to zero (i.e., 95% confidence interval does not contain zero), and the corresponding R^2 values. Using σ_z, for the surfaces without sediment cover there are only four out of 28 combinations of surface and grain size where there is a significant relationship between D/σ_z and pivot angle at the scale of individual measurement cells (Figure 9a, and examples in Figure 9b,c). For surfaces with sediment cover, seven combinations of surfaces and grain size give a significant relationship, primarily for surface S1 (Figure 9a,d). Furthermore, although we would have expected negative relationships between pivot angle and D/σ_z, we actually see positive relationships in three out of 11 cases, such as in Figure 9(b).

Using $\overline{\sigma}_{z\_1win}$, there is still a large proportion of scenarios where there is no relationship between D/roughness and mean cell pivot angle (Figure 9a). Relationships with the highest R^2 occur at smaller filter sizes for surfaces R1$_{rot}$ and S1 with 25% and 50% 11 mm alluvial cover (Figure 9a). Many relationships for surfaces S1, M1, M2 and M2$_{x2}$ are positive, contrary to expectations. We then combined $\overline{\sigma}_{z\_1win}$ with an inclination index (I) that identifies whether each cell slopes upstream or downstream. Using the combined index ($\overline{\sigma}_{z\_1win}I$)
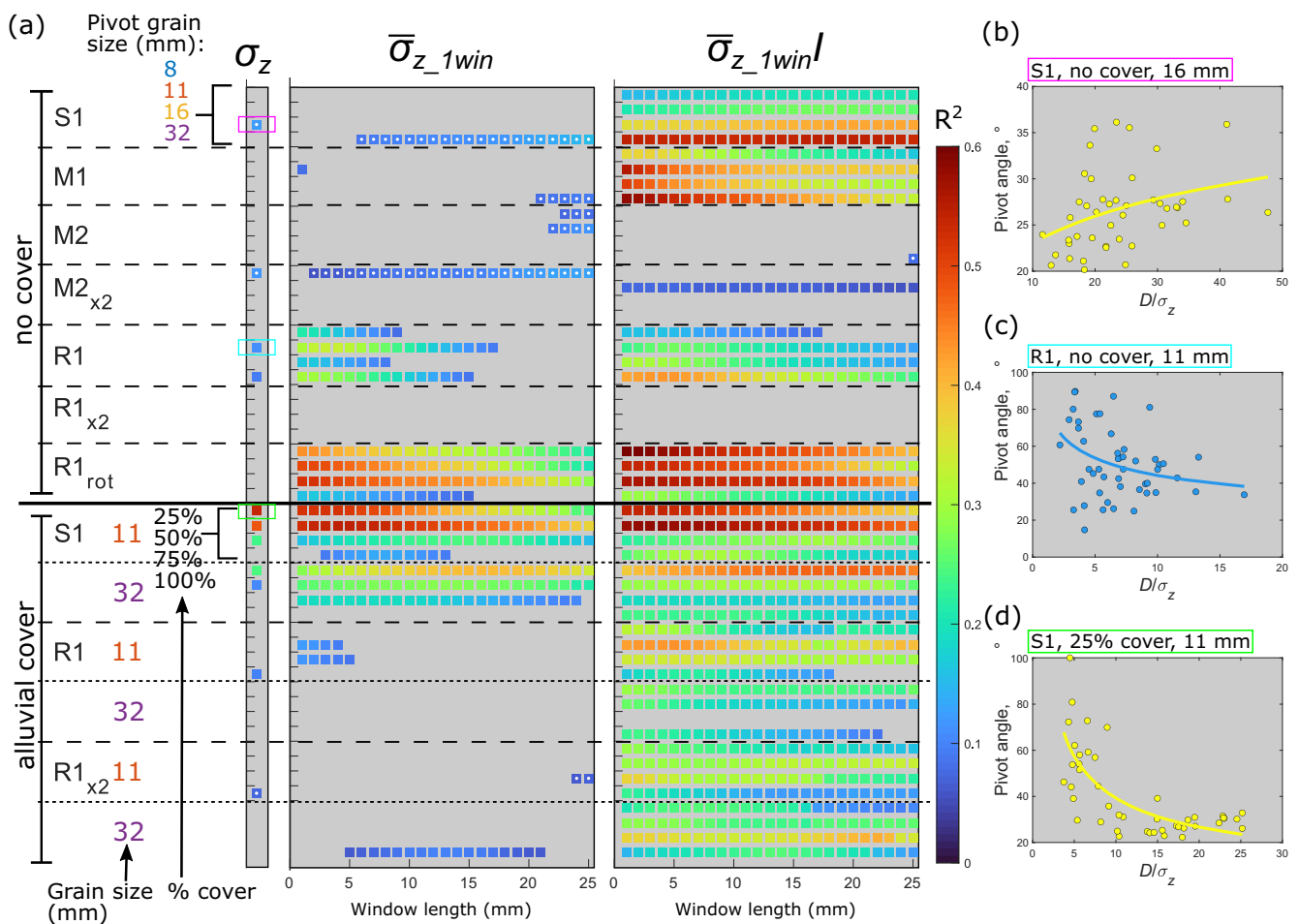
FIGURE 9 (a) The values of R^2 for the power law relationship between grain size divided by cell roughness properties and the mean pivot angle measured for each cell. Cell roughness for each cell is measured using σ_z, $\overline{\sigma}_{z\_1win}$, and $\overline{\sigma}_{z\_1win}I$ ($\overline{\sigma}_{z\_1win}$ combined with inclination index I). Colour shows the R^2 value, and grey areas indicate that the exponent on the power law fit was not significantly different to zero (95% confidence interval includes zero). White dots indicate that the significant relationship is positive, all others are negative. (b–d) The data and power law fits referred to in the coloured boxes in (a), in which roughness is calculated using σ_z [Color figure can be viewed at wileyonlinelibrary.com]

increases the number of significant relationships that are identified, with significant relationships for most surfaces with sediment cover. Furthermore, only one significant relationship is negative. However, some uncovered surfaces (M2, M2$_{x2}$ and R1$_{x2}$) still do not show significant relationships for most grain sizes (Figure 9a). Across all sets of analysis, there is no consistent pattern in the window size that produces the highest R^2. We also repeated this analysis using $\overline{\sigma}_{z\_dir}$ instead of $\overline{\sigma}_{z\_1win}$, and found a very similar set of patterns to those seen in Figure 9(a).

4 | DISCUSSION

4.1 | Interactions between surface roughness and sediment cover

Being able to predict how sediment cover development changes channel roughness is necessary for predicting both hydraulics and sediment transport in bedrock rivers. The simplest approach is to assume first that the total roughness is a weighted average of the individual roughness of bedrock areas and alluvial patches, and second that the roughness of each can be quantified by a roughness length scale (Inoue et al., 2014; Johnson, 2014; Nelson et al., 2014; Nelson & Seminara, 2012). Under these assumptions, in a clast-smooth scenario where D/σ_z or D/R_z is greater than one, then developing sediment cover increases overall roughness. However, our results contradict both of these assumptions. Firstly, total σ_z was often greater than that of either the alluvial or bedrock patches (Figure 4), and so would not be predicted by a weighted average. Secondly, the underlying bedrock topography still affected σ_z even at 100% cover (Figure 4), and so σ_z of alluvial areas was not solely determined by the grain size. Sediment cover may need to be multiple grains deep before the underlying bedrock topography is not important. The combined effect of these was that overall roughness did not increase in the way expected of clast-smooth scenarios.

We conclude that, under conditions of low sediment cover thickness or supply limited regimes, the impact of sediment cover on overall topographic roughness cannot be fully determined from σ_z and grain size alone. There is a need for new ways to predict the evolving topography and roughness of bedrock-alluvial channels. Current attempts are limited by a lack of data, as there are very few datasets of detailed channel topography under different sediment cover extents. Improved understanding would be a step forward in predicting the flow resistance of these systems, as current predictions of flow resistance (e.g., Ferguson et al., 2019; Fernández et al., 2021; Inoue et al., 2014; Johnson, 2014; Li et al., 2020) typically use the same assumptions as outlined earlier. For example, Ferguson et al. (2019) found that they could use weighted averages of roughness lengths of bedrock bed, walls and sediment cover to match the hydraulic roughness back calculated from flow data. However, it is unclear whether this approach would work in other situations, because of a lack of mechanistic understanding of (a) how changes in sediment cover change channel topography, and (b) whether the impact of that topography on the flow can be described using a single roughness length. Another finding from our data is that the impact of sediment cover on roughness can vary depending on the scale of analysis. For instance, adding sediment cover increased roughness at

wavelengths of less than 35 mm (Figure 5). But, at longer wavelengths, adding sediment cover increased roughness for some combinations of cover grain size and surface (Figure 5d), and decreased roughness for other combinations (Figure 5c). Understanding how sediment cover affects flow and sediment transport also requires understanding of the relevant scale at which roughness should be quantified, which may be different for predicting flow hydraulics compared to sediment transport.

4.2 | Interactions between surface roughness and pivot angles

Our results suggest that the scale of roughness that correlates most with pivot angles is one that is similar to, or smaller than, the size of the grains. Our analysis comparing mean pivot angles to roughness values calculated across the entire DEM showed that the highest R^2 values occurred either at the smallest window sizes ($\overline{\sigma}_{z\_sqwin}$ and $\overline{\sigma}_{z\_1win}$; Figure 8a,d), or from high pass filtering at a length scale comparable to the grain size (σ_z and $\overline{\sigma}_{z\_dir}$; Figure 8a,c). We found that incorporating the directionality of the bed also improves R^2. The difference in pivot angles between surfaces R1 and R1$_{rot}$ indicates that changes in the local flow direction, and hence the direction that the grain moves across the bed, could be another source of variability in grain mobility. Directionality and bed inclination are aspects of the bed topography that have not previously been considered with respect to grain entrainment, and including them may be necessary to improve understanding of grain mobility. These findings explain why the standard approach of predicting pivot angles as a function of D/σ_z (e.g., Johnston et al., 1998) does not fully collapse our data (Figure 7).

In contrast to the analysis on mean pivot angles, trying to find relationships between the topographic properties of individual measurement cells and the pivot angles within those cells is only partially successful. Different surfaces, and different combinations of sediment cover and grain size, do not produce consistent relationships (Figure 9). In some cases, pivot angles unexpectedly decrease as measurement cell roughness increases (Figure 9b). Furthermore, there is no single window size that produces the highest R^2 (Figure 9a). However, this analysis does again show that including the directionality and overall slope of the bed improves R^2. The lack of conclusive relationships could be because, for each combination of cell and measurement grain, there is a large combination of potential grain locations and orientations, which would produce a range of pivot angles. We only measured three pivot angles from each measurement cell and so may not have fully captured the potential variability. More repeat measurements from each cell may start to produce clearer trends between cell topographic properties and pivot angles. From a practical perspective though, the finding that the strongest relationships were between average pivot angles and average bed properties (Figure 8a) is helpful because it means that differences between bedrock surfaces can be predicted without having to be concerned with the details of how grain pocket geometry vary across each surface. However, we do note that a bedrock river channel is likely to feature roughness elements at scales larger than our experimental surfaces, and so a reach-scale value of σ_z should not be used uncritically.

Predictions of pivot angles are needed for predictions of critical shear stress using models such as those of Kirchner et al. (1990), Lamb et al. (2008) and Yager et al. (2018). Yet, evaluating our results is difficult because we are not aware of any other datasets measuring pivot angles in bedrock channels. Compared to data from alluvial channels, our pivot angles are of a comparable magnitude to angles measured using a similar methodology where the pivoting grains were placed and tilted on a fixed alluvial surface (e.g., Kirchner et al., 1990). Pivot angles back calculated from the force required to dislodge a sediment grain from an alluvial bed tend to be higher (e.g., Hodge et al., 2013; Prancevic & Lamb, 2015), as the force often also incorporates the effect of displacing overlying and adjacent grains (Yager et al., 2018), or dislodging cohesive sediment around the grain (Barzilai et al., 2012; Hodge et al., 2013). In the context of alluvial patches on bedrock, our approach, which isolates the effect of pocket geometry on pivot angle, therefore best represents the properties of a grain that is deposited onto an existing sediment patch, rather than the properties of grains that are already within that patch and where their entrainment may require dislodging adjacent grains.

4.3 | Implications of our experimental design

When evaluating the implications of these experiments for rivers, it is necessary to consider the ways in which they are not fully representative of natural channels; specifically, the location and depth of sediment cover, the lack of water working, and the uniform grain size distribution. The locations of sediment cover were determined by assuming that cover will initiate in the areas of the bed with the lowest elevations. Flume experiments have shown that this is a reasonable first approximation, but that sediment deposition is also determined by local flow conditions (Finnegan et al., 2007; Hodge & Hoey, 2016b; Johnson & Whipple, 2007). Our experiments only extended to a sediment layer a single grain diameter thick, and the results show that the underlying bedrock still exerts an influence at 100% cover. However, because we did not extend the experiments to thicker depths, further experiments are required to identify the sediment depth at which this influence will cease.

Our sediment cover was not water worked, meaning it lacks the grain imbrication commonly seen in alluvial deposits (Wohl, 1992). In river channels, the extent of grain imbrication can vary spatially and temporally, and our experiments may better represent 'slackwater sediments', sediment in pools (Hodge et al., 2013), or rapidly deposited sediment in ephemeral channels (Hassan, 2005). Flume experiments (Cooper & Tait, 2009; Kirchner et al., 1990) have shown that water-working causes the deepest pores in the bed surface to be filled in, decreasing pivot angles of grains placed onto the bed. However, this may be less likely to occur had we water worked these beds, as the sediment has a uniform grain size. This uniform grain size is another point of difference to a natural riverbed. Alluvial flume experiments have shown that a wider grain size distribution (GSD) can produce a smoother bed (Ockelford & Haynes, 2013) as the smaller grains can fit into small pore spaces between larger grains. Consequently, we might expect that had we used a mixed GSD, the alluvial roughness and pivot angles could all have been smaller, potentially reducing the differences between the bedrock and alluvial surfaces. A further complication of a mixed GSD is that the GSD can vary between different areas of the sediment cover (Papangelakis et al., 2021). Consequently, the size of grains at any location on the bed, and hence pivot angle, becomes even harder to predict (Prancevic & Lamb, 2015).

5 | CONCLUSION

There is still much uncertainty as to how bedrock topography and sediment cover affect sediment dynamics. In this first of two articles, we have measured how grain pivot angles and surface roughness vary between bedrock surfaces and with varying sediment cover. We find that overall roughness is not a weighted average of individual bedrock and alluvial roughness. On average, pivot angles decrease with increasing grain size relative to the surface roughness; however, surfaces with the same value of D/σ_z can have different average pivot angles. These findings do not agree with some common assumptions about how sediment cover affects roughness and pivot angles. There is a need for new methods for predicting roughness and grain mobility, and our results suggest they should focus on surface roughness at grain- and sub-grain-scales, whilst incorporating surface roughness direction and local bed inclination. Our work has also shown 3D printing is an effective way of replicating bedrock surfaces in laboratory experiments and suggests future work could use flume experiments with 3D printed natural bedrock topography to measure how roughness and critical shear stress change as sediment cover develops.

CONFLICT OF INTEREST
The authors declare no financial interests.

AUTHOR CONTRIBUTIONS
MEHB and RAH jointly designed the study. MEHB processed the topographic data, and completed the initial laboratory data collection. SK undertook further laboratory data collection. MEHB analysed the initial data, and RAH analysed the additional data. MEHB and RAH drafted and revised the article.

DATA AVAILABILITY STATEMENT
The pivot angle and topographic datasets are available on zenodo: https://doi.org/10.5281/zenodo.6798180.

ORCID
Marcus E. H. Buechel https://orcid.org/0000-0002-5047-1631
Rebecca A. Hodge https://orcid.org/0000-0002-8792-8949

REFERENCES

Aberle, J. & Smart, G.M. (2003) The influence of roughness structure on flow resistance on steep slopes. *Journal of Hydraulic Research*, 41(3), 259–269. Available from: https://doi.org/10.1080/00221680309499971

Barzilai, R., Laronne, J.B. & Reid, I. (2012) Effect of changes in fine-grained matrix on bedload sediment transport in a gravel-bed river. *Earth Surface Processes and Landforms*, 441–448(5), 441–448. Available from: https://doi.org/10.1002/esp.3288

Benn, D.I. & Ballantyne, C.K. (1993) The description and representation of particle shape. *Earth Surface Processes and Landforms*, 18(7), 665–672. Available from: https://doi.org/10.1002/esp.3290180709

Bertin, S., Friedrich, H., Delmas, P., Chan, E. & Gimel'farb, G. (2015) Digital stereo photogrammetry for grain-scale monitoring of fluvial surfaces: Error evaluation and workflow optimisation. *ISPRS Journal of Photogrammetry and Remote Sensing*, 101, 193–208. Available from: https://doi.org/10.1016/j.isprsjprs.2014.12.019

Bertin, S., Groom, J. & Friedrich, H. (2017) Isolating roughness scales of gravel-bed patches. *Water Resources Research*, 53(8), 6841–6856. Available from: https://doi.org/10.1002/2016WR020205

Brunsden, D. & Thornes, J.B. (1979) Landscape sensitivity and change. *Transactions of the Institute of British Geographers*, 4(4), 463–484. Available from: https://doi.org/10.2307/622210

Buffington, J.M., Dietrich, W.E. & Kirchner, J.W. (1992) Friction angle measurements on a naturally formed gravel streambed: Implications for critical boundary shear stress. *Water Resources Research*, 28(2), 411–425. Available from: https://doi.org/10.1029/91WR02529

Burbank, D.W., Leland, J., Fielding, E., Anderson, R.S., Brozovic, N., Reid, M.R. & Duncan, C. (1996) Bedrock incision, rock uplift and threshold hillslopes in the northwestern Himalayas. *Nature*, 379(6565), 505–510. Available from: https://doi.org/10.1038/379505a0

Butler, J.B., Lane, S.N. & Chandler, J.H. (2001) Characterization of the structure of river-bed gravels using two-dimensional fractal analysis. *Mathematical Geology*, 33, 301–330. Available from: https://doi.org/10.1023/A:1007686206695

Carbonneau, P.E. & Dietrich, J.T. (2017) Cost-effective non-metric photogrammetry from consumer-grade sUAS: Implications for direct georeferencing of structure from motion photogrammetry. *Earth Surface Processes and Landforms*, 42, 473–486. Available from: https://doi.org/10.1002/esp.4012

Chatanantavet, P. & Parker, G. (2008) Experimental study of bedrock channel alluviation under varied sediment supply and hydraulic conditions. *Water Resources Research*, 44(12), 1–19. Available from: https://doi.org/10.1029/2007WR006581

Cooper, J.R. & Tait, S.J. (2009) Water-worked gravel beds in laboratory flumes - a natural analogue? *Earth Surface Processes and Landforms*, 34(3), 384–397. Available from: https://doi.org/10.1002/esp.1743

Durand, M., Chen, C., de Moraes Frasson, R.P., Pavelsky, T.M., Williams, B., Yang, X. & Fore, A. (2020) How will radar layover impact SWOT measurements of water surface elevation and slope, and estimates of river discharge? *Remote Sensing of Environment*, 247, 111883. Available from: https://doi.org/10.1016/j.rse.2020.111883

Ferguson, R.I., Hardy, R.J. & Hodge, R.A. (2019) Flow resistance and hydraulic geometry in bedrock rivers with multiple roughness length scales. *Earth Surface Processes and Landforms*, 44(12), 2437–2449. Available from: https://doi.org/10.1002/esp.4673

Ferguson, R.I., Sharma, B.P., Hodge, R.A., Hardy, R.J. & Warburton, J. (2017) Bed load tracer mobility in a mixed bedrock/alluvial channel. *Journal of Geophysical Research: Earth Surface*, 122(4), 807–822. Available from: https://doi.org/10.1002/2016JF003946

Fernández, R., Vitale, A.J., Parker, G. & García, M.H. (2021) Hydraulic resistance in mixed bedrock-alluvial meandering channels. *Journal of Hydraulic Research*, 59(2), 298–313. Available from: https://doi.org/10.1080/00221686.2020.1780489

Finnegan, N.J., Sklar, L.S. & Fuller, T.K. (2007) Interplay of sediment supply, river incision, and channel morphology revealed by the transient evolution of an experimental bedrock channel. *Journal of Geophysical Research*, 112(F3), F03S11. Available from: https://doi.org/10.1029/2006JF000569

Gilbert, G.K. (1877) *Report on the geology of the Henry Mountains*. Washington: US Government Printing Office 10.5962/bhl.title.51652.

Goode, J.R. & Wohl, E. (2010) Coarse sediment transport in a bedrock channel with complex bed topography. *Water Resources Research*, 46(11), 1–14. Available from: https://doi.org/10.1029/2010WR009078

Hartshorn, K. (2002) Climate-driven bedrock incision in an active Mountain Belt. *Science*, 297(5589), 2036–2038. Available from: https://doi.org/10.1126/science.1075078

Harvey, A.M. (2001) Coupling between hillslopes and channels in upland fluvial systems: Implications for landscape sensitivity, illustrated from the Howgill fells, Northwest England. *Catena*, 42(2-4), 225–250. Available from: https://doi.org/10.1016/S0341-8162(00)00139-9

Hassan, M.A. (2005) Characteristics of Gravel Bars in Ephemeral Streams. *Journal of Sedimentary Research*, 75, 29–42. Available from: https://doi.org/10.2110/jsr.2005.004

Hodge, R., Brasington, J. & Richards, K. (2009) Analysing laser-scanned digital terrain models of gravel bed surfaces: Linking morphology to sediment transport processes and hydraulics. *Sedimentology*, 56(7), 2024–2043. Available from: https://doi.org/10.1111/j.1365-3091.2009.01068.x

Hodge, R.A. & Buechel, M.E.H. (2022) The influence of bedrock river morphology and alluvial cover on gravel entrainment: Part 2. Modelling critical shear stress. *Earth Surface Processes and Landforms*. 2022. Available from: https://doi.org/10.1002/esp.5462

Hodge, R.A. & Hoey, T.B. (2016a) A Froude-scaled model of a bedrock-alluvial channel reach: 1. Hydraulics. *Journal of Geophysical Research: Earth Surface*, 121(9), 1578–1596. Available from: https://doi.org/10.1002/2015JF003706

Hodge, R.A. & Hoey, T.B. (2016b) A Froude-scaled model of a bedrock-alluvial channel reach: 2. Sediment cover. *Journal of Geophysical Research: Earth Surface*, 121(9), 1597–1618. Available from: https://doi.org/10.1002/2015JF003709

Hodge, R.A., Hoey, T.B. & Sklar, L.S. (2011) Bed load transport in bedrock rivers: The role of sediment cover in grain entrainment, translation, and deposition. *Journal of Geophysical Research: Earth Surface*, 116(F4), 1–19. Available from: https://doi.org/10.1029/2011JF002032

Hodge, R.A., Sear, D.A. & Leyland, J. (2013) Spatial variations in surface sediment structure in riffle–pool sequences: A preliminary test of the differential sediment entrainment hypothesis (DSEH). *Earth Surface Processes and Landforms*, 38(5), 449–465. Available from: https://doi.org/10.1002/esp.3290

Hodge, R.A., Voepel, H., Leyland, J., Sear, D.A. & Ahmed, S. (2020) X-ray computed tomography reveals that grain protrusion controls critical shear stress for entrainment of fluvial gravels. *Geology*, 48(2), 149–153. Available from: https://doi.org/10.1130/G46883.1

Hugenholtz, C.H., Whitehead, K., Brown, O.W., Barchyn, T.E., Moorman, B.J., LeClair, A. et al. (2013) Geomorphological mapping with a small unmanned aircraft system (sUAS): Feature detection and accuracy assessment of a photogrammetrically-derived digital terrain model. *Geomorphology*, 194, 16–24. Available from: https://doi.org/10.1016/j.geomorph.2013.03.023

Inoue, T., Izumi, N., Shimizu, Y. & Parker, G. (2014) Interaction among alluvial cover, bed roughness, and incision rate in purely bedrock and alluvial-bedrock channel. *Journal of Geophysical Research: Earth Surface*, 119(10), 2123–2146. Available from: https://doi.org/10.1002/2014JF003133

James, M.R. & Robson, S. (2014) Mitigating systematic error in topographic models derived from UAV and ground-based image networks. *Earth Surface Processes and Landforms*, 39(10), 1413–1420. Available from: https://doi.org/10.1002/esp.3609

Javernick, L., Brasington, J. & Caruso, B. (2014) Modeling the topography of shallow braided rivers using structure-from-motion photogrammetry. *Geomorphology*, 213, 166–182. Available from: https://doi.org/10.1016/j.geomorph.2014.01.006

Johnson, J.P. & Whipple, K.X. (2007) Feedbacks between erosion and sediment transport in experimental bedrock channels. *Earth Surface*

Processes and Landforms, 32(7), 1048–1062. Available from: https://doi.org/10.1002/esp.1471

Johnson, J.P.L. (2014) A surface roughness model for predicting alluvial cover and bed load transport rate in bedrock channels. *Journal of Geophysical Research: Earth Surface*, 119(10), 2147–2173. Available from: https://doi.org/10.1002/2013JF003000

Johnson, J.P.L. & Whipple, K.X. (2010) Evaluating the controls of shear stress, sediment supply, alluvial cover, and channel morphology on experimental bedrock incision rate. *Journal of Geophysical Research: Earth Surface*, 115(F2), 1–21. Available from: https://doi.org/10.1029/2009JF001335

Johnson, J.P.L., Whipple, K.X. & Sklar, L.S. (2010) Contrasting bedrock incision rates from snowmelt and flash floods in the Henry Mountains, Utah. *Bulletin of the Geological Society of America*, 122(9-10), 1600–1615. Available from: https://doi.org/10.1130/B30126.1

Johnston, C.E., Andrews, E.D. & Pitlick, J. (1998) In situ determination of particle friction angles of fluvial gravels. *Water Resources Research*, 34(8), 2017–2030. Available from: https://doi.org/10.1029/98WR00312

Kazhdan, M. & Hoppe, H. (2013) Screened poisson surface reconstruction. *ACM Transactions on Graphics*, 32(3), 1–13. Available from: https://doi.org/10.1145/2487228.2487237

Kirchner, J.W., Dietrich, W.E., Iseya, F. & Ikeda, H. (1990) The variability of critical shear stress, friction angle, and grain protrusion in water-worked sediments. *Sedimentology*, 37(4), 647–672. Available from: https://doi.org/10.1111/j.1365-3091.1990.tb00627.x

Komar, P.D. & Li, Z. (1986) Pivoting analyses of the selective entrainment of sediments by shape and size with application to gravel threshold. *Sedimentology*, 33(3), 425–436. Available from: https://doi.org/10.1111/j.1365-3091.1986.tb00546.x

Lamb, M.P., Brun, F. & Fuller, B.M. (2017) Direct measurements of lift and drag on shallowly submerged cobbles in steep streams: Implications for flow resistance and sediment transport. *Water Resources Research*, 53(9), 7607–7629. Available from: https://doi.org/10.1002/2017WR020883

Lamb, M.P., Dietrich, W.E. & Venditti, J.G. (2008) Is the critical Shields stress for incipient sediment motion dependent on channel-bed slope? *Journal of Geophysical Research*, 113(F2), F02008. Available from: https://doi.org/10.1029/2007JF000831

Li, T., Fuller, T.K., Sklar, L.S., Gran, K.B. & Venditti, J.G. (2020) A mechanistic model for lateral erosion of Bedrock Channel banks by bedload particle impacts. *Journal of Geophysical Research: Earth Surface*, 125(6), e2019JF005509. Available from: https://doi.org/10.1029/2019JF005509

Li, Z. & Komar, P.D. (1986) Laboratory measurements of pivoting angles for applications to selective entrainment of gravel in a current. *Sedimentology*, 33(3), 413–423. Available from: https://doi.org/10.1111/j.1365-3091.1986.tb00545.x

Lowe, D.G. (2004) Distinctive image features from scale-invariant keypoints. *International Journal of Computer Vision*, 60(2), 91–110. Available from: https://doi.org/10.1023/B:VISI.0000029664.99615.94

Mao, L., Cooper, J.R. & Frostick, L.E. (2011) Grain size and topographical differences between static and mobile Armour layers. *Earth Surface Processes and Landforms*, 36(10), 1321–1334. Available from: https://doi.org/10.1002/esp.2156

Montgomery, D.R. & Gran, K.B. (2001) Downstream variations in the width of bedrock channels. *Water Resources Research*, 37(6), 1841–1846. Available from: https://doi.org/10.1029/2000WR900393

Murphy, B.P., Johnson, J.P.L., Gasparini, N.M. & Sklar, L.S. (2016) Chemical weathering as a mechanism for the climatic control of bedrock river incision. *Nature*, 532(7598), 223–227. Available from: https://doi.org/10.1038/nature17449

Nelson, P.A., Bolla Pittaluga, M. & Seminara, G. (2014) Finite amplitude bars in mixed bedrock-alluvial channels. *Journal of Geophysical Research: Earth Surface*, 119(3), 566–587. Available from: https://doi.org/10.1002/2013JF002957

Nelson, P.A. & Seminara, G. (2012) A theoretical framework for the morphodynamics of bedrock channels. *Geophysical Research Letters*,

39(6), L06408. Available from: https://doi.org/10.1029/2011GL050806

Nikora, V.I., Goring, D.G. & Biggs, B.J.F. (1998) On gravel-bed roughness characterization. *Water Resources Research*, 34(3), 517–527. Available from: https://doi.org/10.1029/97WR02886

Ockelford, A.-M. & Haynes, H. (2013) The impact of stress history on bed structure. *Earth Surface Processes and Landforms*, 38(7), 717–727. Available from: https://doi.org/10.1002/esp.3348

Papangelakis, E., Welber, M., Ashmore, P. & MacVicar, B. (2021) Controls of alluvial cover formation, morphology, and bedload transport in a sinuous channel with a non-alluvial boundary. *Earth Surface Processes and Landforms*, 46(2), 399–416. Available from: https://doi.org/10.1002/esp.5032

Pearson, E., Smith, M.W., Klaar, M.J. & Brown, L.E. (2017) Can high resolution 3D topographic surveys provide reliable grain size estimates in gravel bed rivers? *Geomorphology*, 293, 143–155. Available from: https://doi.org/10.1016/j.geomorph.2017.05.015

Powell, D.M. (1998) Patterns and processes of sediment sorting in gravel-bed rivers. *Progress in Physical Geography*, 22(1), 1–32. Available from: https://doi.org/10.1177/030913339802200101

Powell, D.M., Ockelford, A., Rice, S.P., Hillier, J.K., Nguyen, T., Reid, I. et al. (2016) Structural properties of mobile armors formed at different flow strengths in gravel-bed rivers. *Journal of Geophysical Research: Earth Surface*, 121(8), 1494–1515. Available from: https://doi.org/10.1002/2015JF003794

Prancevic, J.P. & Lamb, M.P. (2015) Particle friction angles in steep mountain channels. *Journal of Geophysical Research: Earth Surface*, 120(2), 242–259. Available from: https://doi.org/10.1002/2014JF003286

Reid, E. (2016) *An evaluation of GIS analysis for building a topography of a Bedrock River channel using terrestrial laser scanning*, MSc. Glasgow, UK: University of Glasgow.

Robert, A. (1991) Fractal properties of simulated bed profiles in coarse-grained channels. *Mathematical Geology*, 23(3), 367–382. Available from: https://doi.org/10.1007/BF02065788

Rosnell, T. & Honkavaara, E. (2012) Point cloud generation from aerial image data acquired by a quadrocopter type micro unmanned aerial vehicle and a digital still camera. *Sensors*, 12(1), 453–480. Available from: https://doi.org/10.3390/s120100453

Ružić, I., Marović, I., Benac, Č. & Ilić, S. (2014) Coastal cliff geometry derived from structure-from-motion photogrammetry at Stara Baška, Krk Island, Croatia. *Geo-Marine Letters*, 34(6), 555–565. Available from: https://doi.org/10.1007/s00367-014-0380-4

Schmeeckle, M.W., Nelson, J.M. & Shreve, R.L. (2007) Forces on stationary particles in near-bed turbulent flows. *Journal of Geophysical Research: Earth Surface*, 112(F2), 1–21. Available from: https://doi.org/10.1029/2006JF000536

Shields, A. (1936) Anwendung der Aehnlichkeitsmechanik und der Turbulenzforschung auf die Geschiebebewegung. *Mitteilungen der Preußischen Versuchsanstalt für Wasserbau (in German). Vol. 26.* Berlin: Preußische Versuchsanstalt für Wasserbau.

Sklar, L.S. & Dietrich, W.E. (2001) Sediment and rock strength controls on river incision into bedrock. *Geology*, 29(12), 1087–1090. Available from: https://doi.org/10.1130/0091-7613(2001)029%3C1087:SARSCO%3E2.0.CO;2

Sklar, L.S. & Dietrich, W.E. (2004) A mechanistic model for river incision into bedrock by saltating bed load. *Water Resources Research*, 40(6), W06301. Available from: https://doi.org/10.1029/2003WR002496

Snavely, N., Seitz, S.M. & Szeliski, R. (2008) Modeling the world from internet photo collections. *International Journal of Computer Vision*, 80(2), 189–210. Available from: https://doi.org/10.1007/s11263-007-0107-3

Stumpf, A., Malet, J.P., Allemand, P., Pierrot-Deseilligny, M. & Skupinski, G. (2015) Ground-based multi-view photogrammetry for the monitoring of landslide deformation and erosion. *Geomorphology*, 231, 130–145. Available from: https://doi.org/10.1016/j.geomorph.2014.10.039

Tinkler, K.J. & Wohl, E.E. (1998) *Rivers over rock: Fluvial processes in bedrock channels*. Washington, D. C.: American Geophysical Union https://doi.org/10.1029/GM107.

Turowski, J.M., Hovius, N., Wilson, A. & Horng, M.J. (2008) Hydraulic geometry, river sediment and the definition of bedrock channels.

Geomorphology, 99(1-4), 26–38. Available from: https://doi.org/10.1016/j.geomorph.2007.10.001

Vollmer, S. & Kleinhans, M.G. (2007) Predicting incipient motion, including the effect of turbulent pressure fluctuations in the bed. *Water Resources Research*, 43(5), 1–16. Available from: https://doi.org/10.1029/2006WR004919

Williams, R., Reid, E. & Roberts, K. (2022) Topographicpoint cloud of a bedrock reach of the River Garry, Scotland. [Data Collection] Datacite. Available from: https://doi.org/10.5525/gla.researchdata.1339

Wilson, A., Hovius, N. & Turowski, J.M. (2013) Upstream-facing convex surfaces: Bedrock bedforms produced by fluvial bedload abrasion. *Geomorphology*, 180–181, 187–204. Available from: https://doi.org/10.1016/j.geomorph.2012.10.010

Wohl, E.E. (1992) Bedrock benches and boulder bars: Floods in the Burdekin gorge of Australia. *Geological Society of America Bulletin*, 104(6), 770–778. Available from: https://doi.org/10.1130/0016-7606(1992)104<0770:BBABBF>2.3.CO;2

Wohl, E.E. & Merritt, D.M. (2001) Bedrock channel morphology. *Geological Society of America Bulletin*, 113(9), 1205–1212. Available from: https://doi.org/10.1130/0016-7606(2001)113%3C1205:BCM%3E2.0.CO;2

Yager, E.M., Venditti, J.G., Smith, H.J. & Schmeeckle, M.W. (2018) The trouble with shear stress. *Geomorphology*, 323, 41–50. Available from: https://doi.org/10.1016/j.geomorph.2018.09.008

Zhang, L., Parker, G., Stark, C.P., Inoue, T., Viparelli, E., Fu, X. & Izumi, N. (2015) Macro-roughness model of bedrock–alluvial river morphodynamics. *Earth Surface Dynamics*, 3(1), 113–138. Available from: https://doi.org/10.5194/esurf-3-113-2015